



Cite this: *Energy Environ. Sci.*, 2016, 9, 2789

Received 21st June 2016,  
Accepted 19th July 2016

DOI: 10.1039/c6ee01786j

www.rsc.org/ees

## Engineering water dissociation sites in MoS<sub>2</sub> nanosheets for accelerated electrocatalytic hydrogen production†

Jian Zhang,<sup>a</sup> Tao Wang,<sup>b</sup> Pan Liu,<sup>cd</sup> Shaohua Liu,<sup>a</sup> Renhao Dong,<sup>a</sup> Xiaodong Zhuang,<sup>a</sup> Mingwei Chen<sup>cd</sup> and Xinliang Feng<sup>\*a</sup>

Earth-abundant MoS<sub>2</sub> is widely reported as a promising HER electrocatalyst in acidic solutions, but it exhibits extremely poor HER activities in alkaline media due to the slow water dissociation process. Here we present a combined theoretical and experimental approach to improve the sluggish HER kinetics of MoS<sub>2</sub> electrocatalysts through engineering the water dissociation sites by doping Ni atoms into MoS<sub>2</sub> nanosheets. The Ni sites thus introduced can effectively reduce the kinetic energy barrier of the initial water-dissociation step and facilitate the desorption of the <sup>-</sup>OH that are formed. As a result, the developed Ni-doped MoS<sub>2</sub> nanosheets (Ni-MoS<sub>2</sub>) show an extremely low HER overpotential of ~98 mV at 10 mA cm<sup>-2</sup> in 1 M KOH aqueous solution, which is superior to those (>220 mV at 10 mA cm<sup>-2</sup>) of reported MoS<sub>2</sub> electrocatalysts.

With its high energy density and environmentally friendly advantages, molecular hydrogen has been widely regarded as one of the most promising energy carriers.<sup>1</sup> The scalable and sustainable production of hydrogen fuel through efficient and cost-effective electrocatalytic/photocatalytic/photoelectrocatalytic water splitting technologies, *e.g.*, water-alkali and chlor-alkali electrolyzers, is highly promising as a means to meet the future global energy demands.<sup>2</sup> To this end, active, durable, and earth-abundant electrocatalysts are essential to lower the kinetic overpotentials of the hydrogen evolution reaction (HER) and ultimately accelerate hydrogen production in alkaline solutions.<sup>3</sup> Platinum (Pt) has been acknowledged as the most active and stable HER electrocatalyst with a

### Broader context

Enhancing the sluggish kinetics of the electrocatalytic hydrogen evolution reaction (HER) in water-alkali electrolyzers is pivotal for large-scale and sustainable hydrogen production. Earth-abundant MoS<sub>2</sub> is widely reported as a promising HER electrocatalyst in acidic solutions, but it exhibits extremely poor HER activities in alkaline media due to the slow water dissociation process. Here we present a combined theoretical and experimental approach to improve the sluggish HER kinetics of MoS<sub>2</sub> electrocatalysts through engineering the water dissociation sites by doping Ni atoms into MoS<sub>2</sub> nanosheets. The Ni sites thus introduced can effectively reduce the kinetic energy barrier of the initial water-dissociation step and facilitate the desorption of the <sup>-</sup>OH intermediates that are formed. As a result, the developed Ni-doped MoS<sub>2</sub> nanosheets (Ni-MoS<sub>2</sub>) show a highly competitive HER performance as compared to other state-of-the-art HER electrocatalysts. Therefore, this work opens up a favorable direction for exploring efficient and robust water-splitting electrocatalysts.

near-zero onset overpotential.<sup>4</sup> Unfortunately, the large-scale utilization of Pt catalysts in H<sub>2</sub>-production electrolyzers is seriously hampered by its scarcity and cost.

In regard to its elemental abundance, high activity, and electrochemical stability, molybdenum disulfide (MoS<sub>2</sub>) is a promising catalyst for the electrocatalytic and photocatalytic HER.<sup>5</sup> Recently, both density functional theory (DFT) calculations and experimental results have demonstrated that the electrocatalytic HER activity of crystalline MoS<sub>2</sub> catalysts originates from the unsaturated Mo-S sites along the edges.<sup>6</sup> Inspired by this fundamental understanding, extensive efforts have been dedicated to increasing the number of exposed active sites on MoS<sub>2</sub> catalysts by engineering the nanostructures, *e.g.*, double-gyroid mesoporous MoS<sub>2</sub> films,<sup>6</sup> vertically aligned MoS<sub>2</sub> films,<sup>8</sup> defect-rich MoS<sub>2</sub> nanosheets,<sup>9</sup> amorphous MoS<sub>x</sub> films,<sup>10</sup> [Mo<sub>3</sub>S<sub>13</sub>]<sup>2-</sup> clusters,<sup>11</sup> and CoS<sub>x</sub>/MoS<sub>x</sub> hybrids.<sup>12</sup> Unfortunately, although the MoS<sub>2</sub>-based electrocatalysts thus developed exhibit enhanced HER activities in acidic solutions, the HER kinetics in alkaline electrolytes still suffer from a high overpotential (>220 mV at a current of 10 mA cm<sup>-2</sup>).<sup>12</sup> The high kinetic energy barrier of

<sup>a</sup> Center for Advancing Electronics Dresden (cfaed) & Department of Chemistry and Food Chemistry, Technische Universität Dresden, 01062 Dresden, Germany.  
E-mail: xinliang.feng@tu-dresden.de

<sup>b</sup> Université Lyon, Ens de Lyon, CNRS, Université Lyon 1, Laboratoire de Chimie, UMR 5182, F-69342, Lyon, France

<sup>c</sup> WPI Advanced Institute for Materials Research, Tohoku University, Sendai 980-8577, Japan

<sup>d</sup> CREST, JST, 4-1-8 Honcho Kawaguchi, Saitama 332-0012, Japan

† Electronic supplementary information (ESI) available. See DOI: 10.1039/c6ee01786j



the initial water dissociation process (the Volmer step) and the strong adsorption of the formed  $\text{OH}^-$  on the surfaces of  $\text{MoS}_2$  are responsible for the sluggish HER kinetics in alkaline solutions.<sup>13</sup>

Herein, we demonstrate a novel strategy to efficiently speed up the sluggish HER kinetics of  $\text{MoS}_2$  electrocatalysts through doping Ni atoms into crystalline  $\text{MoS}_2$  nanosheets. The DFT calculations reveal the fact that the kinetic energy barrier of the initial water dissociation step and the adsorption interaction of  $\text{OH}^-$  are substantially reduced on Ni-doped  $\text{MoS}_2$  catalysts ( $\text{Ni-MoS}_2$ ). Accordingly,  $\text{Ni-MoS}_2$  nanosheets with a chemical composition of  $\text{Ni}_{0.13}\text{Mo}_{0.87}\text{S}_2$  were prepared on carbon cloth *via* a one-pot hydrothermal reaction. The resultant  $\text{Ni-MoS}_2$  nanosheets exhibit an excellent electrochemical HER activity in 1 M KOH aqueous solution with an extremely low overpotential of  $\sim 98$  mV at a current density of  $10 \text{ mA cm}^{-2}$ . The achieved overpotential is much lower than those of reported  $\text{MoS}_2$  electrocatalysts (overpotential is  $> 220$  mV at  $10 \text{ mA cm}^{-2}$  in basic solutions and  $\geq 110$  mV at  $10 \text{ mA cm}^{-2}$  in acidic solutions).<sup>12,14</sup>

The kinetic energy barriers of the prior water dissociation step ( $\Delta G(\text{H}_2\text{O})$ , Volmer step), the Gibbs free energy of adsorbed  $\text{OH}^-$  ( $G(\text{OH})$ ), and the concomitant combination of  $\text{H}^*$  intermediates into molecular hydrogen ( $\Delta G(\text{H})$ , Tafel step) were firstly investigated using the DFT calculations according to the as-built catalyst models including  $\text{MoS}_2$ ,  $\text{Ni-MoS}_2$ , Co-doped  $\text{MoS}_2$  ( $\text{Co-MoS}_2$ ), and Fe-doped  $\text{MoS}_2$  ( $\text{Fe-MoS}_2$ ) (Fig. S1, ESI<sup>†</sup>). As shown in Fig. 1 and Table S1 (ESI<sup>†</sup>),  $\text{MoS}_2$  exhibits a very high  $\Delta G(\text{H}_2\text{O})$  up to 1.17 eV and an extremely low  $G(\text{OH})$  ( $-5.24$  eV). Substituting a Mo atom with a metal (Ni, Co, or Fe) atom along the edge of  $\text{MoS}_2$  dramatically decreases the  $\Delta G(\text{H}_2\text{O})$  value in the order of:  $\text{Ni-MoS}_2$  ( $\Delta G(\text{H}_2\text{O}) = 0.66$  eV)  $<$   $\text{Co-MoS}_2$  ( $\Delta G(\text{H}_2\text{O}) = 0.76$  eV)  $<$   $\text{Fe-MoS}_2$  ( $\Delta G(\text{H}_2\text{O}) = 0.96$  eV). In contrast to  $\text{MoS}_2$ , the  $G(\text{OH})$  value is reduced to  $-3.46$  eV for  $\text{Ni-MoS}_2$ ,  $-3.46$  eV for  $\text{Co-MoS}_2$ , and  $-3.36$  eV for  $\text{Fe-MoS}_2$ . These greatly reduced  $\Delta G(\text{H}_2\text{O})$  and  $G(\text{OH})$  values on  $\text{Ni-MoS}_2$  suggest that the kinetics of the initial water dissociation step and the concomitant

desorption of the formed  $\text{OH}^-$  can be effectively promoted after the doping of a Ni atom into the edge of  $\text{MoS}_2$ . In addition, the  $\Delta G(\text{H})$  is  $-0.06$  eV for  $\text{Ni-MoS}_2$ ,  $0.13$  eV for  $\text{Co-MoS}_2$ , and  $-0.10$  eV for  $\text{Fe-MoS}_2$ , which are much lower than 0.60 eV for  $\text{MoS}_2$ . The negative value of  $\Delta G(\text{H})$  for  $\text{Ni-MoS}_2$  catalysts shows that the subsequent Tafel step towards molecular hydrogen can spontaneously occur in thermodynamics.

Encouraged by these DFT results, we prepared metal-doped  $\text{MoS}_2$  nanosheets ( $\text{M-MoS}_2$ ), where the metal (Ni, Co, or Fe) atoms are homogeneously doped into the crystalline  $\text{MoS}_2$  nanosheets, as schematically illustrated in Fig. S2 (ESI<sup>†</sup>). Specifically, the  $\text{Ni-MoS}_2$  nanosheets were constructed on carbon cloth ( $1 \times 3 \text{ cm}^2$ ) through a one-pot hydrothermal reaction at  $200^\circ\text{C}$  for 24 h, involving  $\text{NiSO}_4 \cdot 6\text{H}_2\text{O}$ ,  $\text{Na}_2\text{MoO}_4 \cdot 2\text{H}_2\text{O}$ , and  $\text{l-cysteine}$  in 15 mL deionized water. The molar content ( $x$ , expressed in  $\text{Ni}_x\text{Mo}_{1-x}\text{S}_2$ ) of Ni in the as-obtained  $\text{Ni-MoS}_2$  nanosheets could be tuned from 6.2% to 19.1% by adjusting the dosage of  $\text{NiSO}_4 \cdot 6\text{H}_2\text{O}$ . The loading weight of  $\text{Ni-MoS}_2$  nanosheets on the carbon cloth was approximately  $0.89 \text{ mg cm}^{-2}$ . Under the same hydrothermal conditions,  $\text{Co-MoS}_2$  ( $\text{Co}_{0.03}\text{Mo}_{0.97}\text{S}_2$ ) and  $\text{Fe-MoS}_2$  ( $\text{Fe}_{0.12}\text{Mo}_{0.88}\text{S}_2$ ) nanosheets on carbon cloth were also prepared utilizing  $\text{CoSO}_4 \cdot 7\text{H}_2\text{O}$  and  $\text{FeSO}_4 \cdot 7\text{H}_2\text{O}$  as Co and Fe sources, respectively. For comparison, pristine  $\text{MoS}_2$  nanosheets were synthesized through the same process without involving  $\text{NiSO}_4 \cdot 6\text{H}_2\text{O}$ .

The crystalline structure of the  $\text{M-MoS}_2$  nanosheets was first confirmed by X-ray diffraction (XRD) measurements. As shown in Fig. S3 (ESI<sup>†</sup>), the  $\text{Ni-MoS}_2$  nanosheets show the diffraction peaks at diffraction angles similar to semiconducting  $\text{MoS}_2$ .<sup>15</sup> To probe the morphologies of the as-obtained  $\text{Ni-MoS}_2$ , scanning electron microscopy (SEM) and high-resolution transmission electron microscopy (HRTEM) were employed. Fig. 2a and Fig. S4 (ESI<sup>†</sup>) reveal numerous sheet-like nanostructures, which are vertically aligned and inter-connected on the carbon cloth. The thickness and length of the  $\text{Ni-MoS}_2$  nanosheets are approximately 5–10 nm and 40–100 nm, respectively. Elemental mappings of

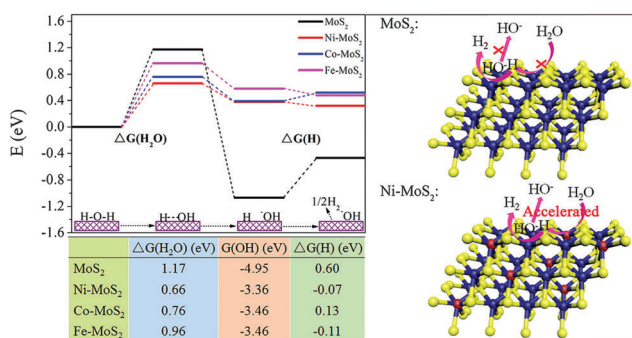


Fig. 1 The results of the DFT calculations and the corresponding mechanisms of the electrocatalytic HER on the surfaces of different catalysts under alkaline conditions.  $\Delta G(\text{H}_2\text{O})$  and  $\Delta G(\text{H})$  are the related kinetic energy barriers for the Volmer and Tafel steps on the catalysts, respectively.  $G(\text{OH})$  is the Gibbs free energy of the adsorbed  $\text{OH}^-$  on the surfaces of catalysts.  $E$  (eV) in the diagram represents the free energies of the different reactive stages. The yellow, blue and red spheres represent S, Mo and Ni, respectively.

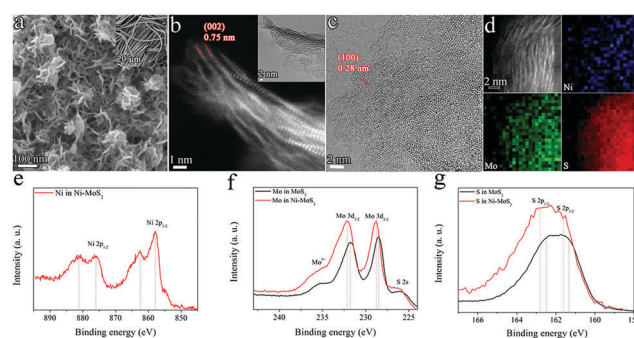


Fig. 2 Morphology and structural characterization of the  $\text{Ni-MoS}_2$  catalysts. (a) SEM and (b and c) HRTEM images of the  $\text{Ni-MoS}_2$  nanosheets; (d) corresponding STEM-EDS chemical mappings of Ni, Mo, and S elements in the  $\text{Ni-MoS}_2$  nanosheets; high-resolution XPS spectra of (e) Ni 2p, (f) Mo 3d, and (g) S 2p in the  $\text{MoS}_2$  and  $\text{Ni-MoS}_2$  nanosheets. The insets in (a and b) are the low-magnification SEM image of the  $\text{Ni-MoS}_2$  nanosheets coated on the carbon cloth and the HRTEM image of the edges of the  $\text{Ni-MoS}_2$  nanosheets, respectively.



field-emission SEM (FE-SEM) reveal the homogenous distributions of Ni, Mo, and S elements over the Ni-MoS<sub>2</sub> nanosheets (Fig. S5a–e, ESI<sup>†</sup>). The corresponding energy dispersive X-ray spectroscopy (EDS) analysis further suggests a chemical elemental composition of Ni<sub>0.13</sub>Mo<sub>0.87</sub>S<sub>2</sub> (Fig. S5f, ESI<sup>†</sup>). Fig. 2b and c show the HRTEM images of the Ni-MoS<sub>2</sub> nanosheets. Lattice fringes with lattice distances of 0.75 and 0.28 nm correspond to the (002) edge and (100) plane facets of the Ni-MoS<sub>2</sub> nanosheets, respectively.<sup>16</sup> Scanning TEM (STEM)-EDS characterization was utilized to analyze the elemental distributions in the Ni-MoS<sub>2</sub> nanosheets (Fig. 2d). Apparently, the Ni atoms are homogeneously distributed in the Ni-MoS<sub>2</sub> nanosheets. Similarly, the morphologies and chemical compositions of the as-prepared MoS<sub>2</sub>, Co-MoS<sub>2</sub>, and Fe-MoS<sub>2</sub> nanosheets were also investigated by SEM, XRD and EDS analyses (Fig. S6–S8, ESI<sup>†</sup>).

X-ray photoelectron spectroscopy (XPS) was applied to probe the composition and valence state of the Ni-MoS<sub>2</sub> nanosheets. The survey spectrum demonstrates a chemical composition of Ni<sub>0.12</sub>Mo<sub>0.88</sub>S<sub>2</sub>, which is consistent with inductively coupled plasma mass spectrometry (ICP-MS) analysis (Ni<sub>0.13</sub>Mo<sub>0.87</sub>S<sub>2</sub>) (Fig. S9–S11, ESI<sup>†</sup>). The peaks of Ni 2p<sub>3/2</sub> and Ni 2p<sub>1/2</sub> were observed at 857.9 eV and 876.0 eV, respectively (Fig. 2e). The binding energies of Mo 3d<sub>5/2</sub> and Mo 3d<sub>3/2</sub> in the Ni-MoS<sub>2</sub> nanosheets shifted to 228.8 and 232.1 eV, respectively (Fig. 2f), in contrast to those (Mo 3d<sub>5/2</sub> at 228.5 and Mo 3d<sub>3/2</sub> at 231.8 eV) in the pristine MoS<sub>2</sub> nanosheets. Likewise, the S 2p<sub>3/2</sub> and S 2p<sub>1/2</sub> signals in the Ni-MoS<sub>2</sub> also have a shift of ~0.3 eV, relative to those in the MoS<sub>2</sub> nanosheets (Fig. 2g and Fig. S9, ESI<sup>†</sup>). Raman spectroscopy was further used to survey the Ni-MoS<sub>2</sub> nanosheets. The characteristic Raman bands of the A<sub>1g</sub> and E<sub>2g</sub> modes of Ni-MoS<sub>2</sub> shifted to 406 and 376 cm<sup>-1</sup>, relative to the MoS<sub>2</sub> nanosheets (A<sub>1g</sub> at 412 cm<sup>-1</sup>; E<sub>2g</sub> at 388 cm<sup>-1</sup>) (Fig. S12, ESI<sup>†</sup>). These XPS and Raman results highlight the strong influence of Ni atom doping on the electronic structure of MoS<sub>2</sub>.

To evaluate the electrocatalytic HER activities of the catalysts, a three-electrode configuration in Ar-saturated 1 M KOH aqueous solution was applied using a Hg/HgO electrode and a graphite rod as the reference and counter electrodes, respectively (Fig. S13, ESI<sup>†</sup>). All potentials are referenced to the reversible hydrogen electrode (RHE) and the ohmic potential drop caused by the solution resistance has been deducted unless noted (Fig. S14, ESI<sup>†</sup>). As shown in Fig. 3a, although MoS<sub>2</sub> can act as a HER catalyst, the hydrogen evolution reaction occurred at an overpotential of ~197 mV and the cathodic current density reached 10 mA cm<sup>-2</sup> at a high overpotential of ~308 mV. Noticeably, the doping of Ni, Co, or Fe atoms into MoS<sub>2</sub> nanosheets leads to profound enhancements of the HER activities. Specifically, Co-MoS<sub>2</sub> and Fe-MoS<sub>2</sub> catalysts show overpotentials of only 203 and 163 mV at a current density of 10 mA cm<sup>-2</sup>, respectively. Remarkably, the onset overpotential of Ni-MoS<sub>2</sub> catalysts was as low as 45 mV and a current density of 10 mA cm<sup>-2</sup> was delivered at an extremely low overpotential of ~98 mV, which is much lower than those of the as-prepared MoS<sub>2</sub> catalysts (~308 mV at 10 mA cm<sup>-2</sup>) and the reported MoS<sub>2</sub>-based catalysts (regardless of whether in basic and acidic solutions)

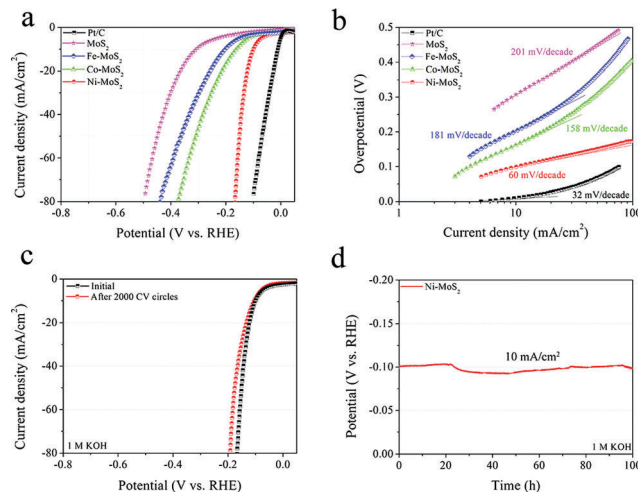


Fig. 3 Electrochemical HER measurements of different catalysts. (a) Polarization curves and (b) corresponding Tafel slopes of the MoS<sub>2</sub>, Ni-MoS<sub>2</sub>, Co-MoS<sub>2</sub>, Fe-MoS<sub>2</sub>, and commercial Pt/C catalysts; (c) CV stability and (d) 100 h operating durability of the Ni-MoS<sub>2</sub> catalysts in 1 M KOH aqueous solution. Scan rate: 1 mV s<sup>-1</sup>.

including amorphous MoS<sub>x</sub> film (~500 mV at 4 mA cm<sup>-2</sup>),<sup>10</sup> MoS<sub>2</sub> nanoparticles grown on graphene (~155 mV at 10 mA cm<sup>-2</sup>),<sup>17</sup> defect-rich MoS<sub>2</sub> nanosheets (~190 mV at 10 mA cm<sup>-2</sup>),<sup>9</sup> double-gyroid mesoporous MoS<sub>2</sub> films (~235 mV at 10 mA cm<sup>-2</sup>),<sup>7</sup> Li-MoS<sub>2</sub> films (~168 mV at 10 mA cm<sup>-2</sup>),<sup>18</sup> and CoS<sub>x</sub>/MoS<sub>2</sub> hybrids (~220 mV at 5 mA cm<sup>-2</sup>)<sup>12</sup> (Table S2, ESI<sup>†</sup>). Moreover, the HER overpotential achieved by the Ni-MoS<sub>2</sub> catalysts is comparable to those of highly active NiO/Ni heterostructures (~80 mV at 10 mA cm<sup>-2</sup>),<sup>19</sup> CoP nanowires on carbon cloth (~209 mV at 10 mA cm<sup>-2</sup>),<sup>20</sup> porous MoC<sub>x</sub> nano-octahedra (~151 mV at 10 mA cm<sup>-2</sup>),<sup>21</sup> cobalt-sulfide films (~180 mV at 10 mA cm<sup>-2</sup>),<sup>22</sup> and CoO/Co/N-doped carbon hybrids (~232 mV at 10 mA cm<sup>-2</sup>)<sup>23</sup> (Table S3, ESI<sup>†</sup>).

Fig. 3b displays Tafel plots of the corresponding polarization curves, which provide further insights into the HER reaction pathways on the surfaces of the catalysts. The Tafel slope of the MoS<sub>2</sub> catalysts is as high as 201 mV per decade. However, the Tafel slope of the Ni-MoS<sub>2</sub> catalysts is significantly decreased to 60 mV per decade. Compared with the MoS<sub>2</sub> catalysts, the greatly decreased Tafel slope highlights that the kinetics of the water dissociation step is effectively facilitated on the Ni-MoS<sub>2</sub> catalysts. On the basis of the Tafel analysis, the exchange current density of the Ni-MoS<sub>2</sub> catalysts was estimated to be ~0.98 mA cm<sup>-2</sup> (Fig. S15, ESI<sup>†</sup>). Meanwhile, the turnover frequency (TOF) of the Ni-MoS<sub>2</sub> catalysts was up to 0.32 s<sup>-1</sup> at an overpotential of 150 mV (Fig. S16, ESI<sup>†</sup>). In addition, the electrochemical impedance spectroscopy (EIS) analyses also confirmed a faster HER kinetic process on the Ni-MoS<sub>2</sub> catalysts than on the MoS<sub>2</sub> catalysts (Fig. S17, ESI<sup>†</sup>).

Electrocatalytic stability is another important criterion for the HER catalysts. For the Ni-MoS<sub>2</sub> catalysts, after 2000 cyclic voltammetry (CV) cycles in 1 M KOH aqueous solution, the overpotential required for a current density of 10 mA cm<sup>-2</sup> increased by only 5 mV (Fig. 3c). A long-term HER process was



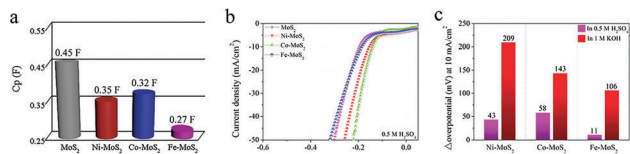


Fig. 4 (a) Electrochemical double layer capacitances of the as-achieved catalysts in 1 M KOH aqueous solution; (b) polarization curves of the catalysts in 0.5 M H<sub>2</sub>SO<sub>4</sub> aqueous solution and (c) the alterations of the HER overpotentials of the catalysts under acidic and basic conditions.

performed at a current density of 10 mA cm<sup>-2</sup> (Video S1, ESI†). Fig. 3d manifests that the Ni-MoS<sub>2</sub> catalysts retained a steady HER activity and no noticeable increase in potential was observed for hydrogen production over a period of 100 h. After the above HER durability assessment, the structural information of the Ni-MoS<sub>2</sub> catalysts was scrutinized using SEM. The morphology of the Ni-MoS<sub>2</sub> catalysts showed no structural variations, suggesting their superior structural stability during the HER process (Fig. S18, ESI†). The electrochemical stability of the Ni-MoS<sub>2</sub> catalysts was further confirmed by element mapping, EDX, and XPS analysis (Fig. S19 and S20, ESI†).

To clarify the influence of the active surface area on the electrocatalytic HER activity, the active surface areas of the as-synthesized catalysts were analyzed through their electrochemical double layer capacitances ( $C_p$ ).<sup>24</sup> For comparison, the  $C_p$  of the MoS<sub>2</sub> catalysts was approximately 0.54 F. However, the Ni-MoS<sub>2</sub>, Co-MoS<sub>2</sub>, and Fe-MoS<sub>2</sub> catalysts showed low  $C_p$  values of ~0.35 F, 0.32 F, and 0.27 F, respectively (Fig. 4a and Fig. S21, ESI†). These results demonstrate that the excellent HER activity of the Ni-MoS<sub>2</sub> catalysts originates from the improved HER kinetics, rather than the active surface area. As illustrated in the reported volcano plots, under acidic conditions, the HER kinetics of a catalyst is strongly correlated with its hydrogen adsorption ability.<sup>6,25</sup> To further understand the roles of hydrogen adsorption and water dissociation in electrocatalytic HER kinetics of the Ni-MoS<sub>2</sub> catalysts, the electrochemical HER activities of the catalysts were tested under acidic conditions. As shown in Fig. 4b and c, in comparison with the MoS<sub>2</sub> catalysts, the HER overpotential of the Ni-MoS<sub>2</sub> catalysts at 10 mA cm<sup>-2</sup> was decreased by only 43 mV in 0.5 M H<sub>2</sub>SO<sub>4</sub> aqueous solution, which was far less than 209 mV in 1 M KOH aqueous solution. These studies clearly manifest that the greatly enhanced HER activity of the Ni-MoS<sub>2</sub> catalysts in 1 M KOH aqueous solution is mainly attributed to the initially accelerated water dissociation, rather than the hydrogen adsorption properties.

We also investigated a series of Ni-MoS<sub>2</sub> catalysts with different molar contents of Ni (Ni-MoS<sub>2-x</sub>;  $x$  is expressed in Ni<sub>x</sub>Mo<sub>1-x</sub>S<sub>2</sub>) in 1 M KOH aqueous solution (Fig. S22, ESI†). As shown in Fig. S23 (ESI†), the HER polarization curves of the Ni-MoS<sub>2</sub> catalysts dramatically shifted towards lower overpotentials along with the increased Ni content. When the molar content of Ni was ~13.3%, the Ni-MoS<sub>2</sub> catalysts exhibited the lowest HER overpotential (~98 mV at 10 mA cm<sup>-2</sup>). The overpotential increased if the molar content of Ni was more than

13.3% and even the overpotential of the NiS<sub>2</sub> catalysts at 10 mA cm<sup>-2</sup> was approximately 201 mV.

In summary, we have demonstrated a novel strategy to greatly accelerate the sluggish HER kinetics of MoS<sub>2</sub> electrocatalysts through engineering the water dissociation sites in alkaline environments. The combined DFT and experimental results show that the doping of Ni atoms into crystalline MoS<sub>2</sub> nanosheets can efficiently lower the kinetic energy barrier of the initial water dissociation step and facilitate the desorption of the formed <sup>-</sup>OH from the surface of the Ni-MoS<sub>2</sub> catalysts. Therefore, this work opens up a favorable direction for exploring efficient and robust water-splitting catalysts, which have promising applications in alkali electrolyzers and solar-driven photocatalytic/photoelectrocatalytic devices.

## Acknowledgements

This work was financially supported by an ERC grant on 2DMA-TER and EC under Graphene Flagship (No. CNECT-ICT-604391). We also acknowledge the Cfaed (Center for Advancing Electronics Dresden) and the Dresden Center for Nanoanalysis (DCN) at TU Dresden. P. L. and M. C. were supported by JST-CREST “Phase Interface Science for Highly Efficient Energy Utilization”, Japan Science and Technology Agency.

## Notes and references

- N. S. Lewis and D. G. Nocera, *Proc. Natl. Acad. Sci. U. S. A.*, 2006, **103**, 15729.
- K. Zeng and D. Zhang, *Prog. Energy Combust. Sci.*, 2010, **36**, 307; M. G. Walter, E. L. Warren, J. R. McKone, S. W. Boettcher, Q. Mi, E. A. Santori and N. S. Lewis, *Chem. Rev.*, 2010, **110**, 6446; J. S. Zhang, Y. Chen and X. C. Wang, *Energy Environ. Sci.*, 2015, **8**, 3092.
- M. S. Faber and S. Jin, *Energy Environ. Sci.*, 2014, **7**, 3519; C. G. Morales-Guio, L.-A. Stern and X. Hu, *Chem. Soc. Rev.*, 2014, **43**, 6555.
- X. Zou and Y. Zhang, *Chem. Soc. Rev.*, 2015, **44**, 5148; Y. Zheng, Y. Jiao, M. Jaroniec and S. Z. Qiao, *Angew. Chem., Int. Ed.*, 2015, **54**, 52.
- X. Chia, A. Y. S. Eng, A. Ambrosi, S. M. Tan and M. Pumera, *Chem. Rev.*, 2015, **115**, 11941; Q. Lu, Y. Yu, Q. Ma, B. Chen and H. Zhang, *Adv. Mater.*, 2016, **28**, 1917; Y. D. Hou, A. B. Laursen, J. S. Zhang, G. G. Zhang, Y. S. Zhu, X. C. Wang, S. Dahl and I. Chorkendorff, *Angew. Chem., Int. Ed.*, 2013, **52**, 3621; G. Zhang, H. J. Liu, J. H. Qu and J. H. Li, *Energy Environ. Sci.*, 2016, **9**, 1190; X. W. Zhang, F. Meng, S. Mao, Q. Ding, M. J. Shearer, M. S. Faber, J. H. Chen, R. J. Hamers and S. Jin, *Energy Environ. Sci.*, 2015, **8**, 862.
- B. Hinnemann, P. G. Moses, J. Bonde, K. P. Jørgensen, J. H. Nielsen, S. Hørch, I. Chorkendorff and J. K. Nørskov, *J. Am. Chem. Soc.*, 2005, **127**, 5308; T. F. Jaramillo, K. P. Jørgensen, J. Bonde, J. H. Nielsen, S. Hørch and I. Chorkendorff, *Science*, 2007, **317**, 100.
- J. Kibsgaard, Z. Chen, B. N. Reinecke and T. F. Jaramillo, *Nat. Mater.*, 2012, **11**, 963.



- 8 D. Kong, H. Wang, J. J. Cha, M. Pasta, K. J. Koski, J. Yao and Y. Cui, *Nano Lett.*, 2013, **13**, 1341.
- 9 J. Xie, H. Zhang, S. Li, R. Wang, X. Sun, M. Zhou, J. Zhou, X. W. Lou and Y. Xie, *Adv. Mater.*, 2013, **25**, 5807.
- 10 D. Merki, S. Fierro, H. Vrubel and X. Hu, *Chem. Sci.*, 2011, **2**, 1262.
- 11 J. Kibsgaard, T. F. Jaramillo and F. Besenbacher, *Nat. Chem.*, 2014, **6**, 248.
- 12 J. Staszak-Jirkovsky, C. D. Malliakas, P. P. Lopes, N. Danilovic, S. S. Kota, K.-C. Chang, B. Genorio, D. Strmcnik, V. R. Stamenkovic, M. G. Kanatzidis and N. M. Markovic, *Nat. Mater.*, 2015, **15**, 197.
- 13 R. Subbaraman, D. Tripkovic, D. Strmcnik, K.-C. Chang, M. Uchimura, A. P. Paulikas, V. Stamenkovic and N. M. Markovic, *Science*, 2011, **334**, 1256; R. Subbaraman, D. Tripkovic, K.-C. Chang, D. Strmcnik, A. P. Paulikas, P. Hirunsit, M. Chan, J. Greeley, V. Stamenkovic and N. M. Markovic, *Nat. Mater.*, 2012, **11**, 550.
- 14 D. J. Li, U. N. Maiti, J. Lim, D. S. Choi, W. J. Lee, Y. Oh, G. Y. Lee and S. O. Kim, *Nano Lett.*, 2014, **14**, 1228.
- 15 J. Zhang, S. Liu, H. Liang, R. Dong and X. Feng, *Adv. Mater.*, 2015, **27**, 7426.
- 16 J. Miao, F.-X. Xiao, H. B. Yang, S. Y. Khoo, J. Chen, Z. Fan, Y.-Y. Hsu, H. M. Chen, H. Zhang and B. Liu, *Sci. Adv.*, 2015, **1**, e1500259.
- 17 Y. Li, H. Wang, L. Xie, Y. Liang, G. Hong and H. Dai, *J. Am. Chem. Soc.*, 2011, **133**, 7296.
- 18 H. Wang, Z. Lu, S. Xu, D. Kong, J. J. Cha, G. Zheng, P.-C. Hsu, K. Yan, D. Bradshaw, F. B. Prinz and Y. Cui, *Proc. Natl. Acad. Sci. U. S. A.*, 2013, **110**, 19701.
- 19 M. Gong, W. Zhou, M.-C. Tsai, J. Zhou, M. Guan, M.-C. Lin, B. Zhang, Y. Hu, D.-Y. Wang, J. Yang, S. J. Pennycook, B.-J. Hwang and H. Dai, *Nat. Commun.*, 2014, **5**, 4695.
- 20 J. Tian, Q. Liu, A. M. Asiri and X. Sun, *J. Am. Chem. Soc.*, 2014, **136**, 7587.
- 21 H. B. Wu, B. Y. Xia, L. Yu, X.-Y. Yu and X. W. Lou, *Nat. Commun.*, 2015, **6**, 6512.
- 22 Y. Sun, C. Liu, D. C. Grauer, J. Yano, J. R. Long, P. Yang and C. J. Chang, *J. Am. Chem. Soc.*, 2013, **135**, 17699.
- 23 H. Jin, J. Wang, D. Su, Z. Wei, Z. Pang and Y. Wang, *J. Am. Chem. Soc.*, 2015, **137**, 2688.
- 24 M. A. Lukowski, A. S. Daniel, F. Meng, A. Forticaux, L. Li and S. Jin, *J. Am. Chem. Soc.*, 2013, **135**, 10274.
- 25 J. Greeley, T. F. Jaramillo, J. Bonde, I. Chorkendorff and J. K. Nørskov, *Nat. Mater.*, 2006, **5**, 909.

